THE JOURNAL OF PHYSICAL CHEMISTRY C

C: Physical Processes in Nanomaterials and Nanostructures

Polarization Effects of Transversal and Longitudinal Optical Phonons in Bundles of Multi-Wall Carbon Nanotubes

Francesca Ripanti, Giulio D'Acunto, Maria Grazia Betti, Carlo Mariani, Carla Bittencourt, and Paolo Postorino

J. Phys. Chem. C, **Just Accepted Manuscript** • DOI: 10.1021/acs.jpcc.9b02638 • Publication Date (Web): 17 Jul 2019

Polarization Effects of Transversal and Longitudinal Optical Phonons in Bundles of Multi-Wall Carbon Nanotubes

Francesca Ripanti[1], Giulio D'Acunto[1§], Maria Grazia Betti[1], Carlo Mariani[1], Carla Bittencourt[2], Paolo Postorino[1]*

[1] Department of Physics, Sapienza University of Rome, P.le Aldo Moro 2, 00185 Rome, Italy

[2] Chimie des Interactions Plasma-Surface (ChIPS), University of Mons, 20 Place du Parc, 7000 Mons, Belgium

[§] present address: Division of Synchrotron Radiation Research, Lund University, Sölvegatan 14, Lund, Sweden

AUTHOR INFORMATION

Corresponding Author

*Francesca Ripanti: francesca.ripanti@uniroma1.it

ABSTRACT

We report on the polarization analysis of the Raman spectrum of highly vertically aligned multi-wall carbon nanotubes (MWCNTs). A simple model considering the average angle distribution across the MWCNT axes accounts for the observed angular dependent Raman mode intensity. The model fully fits the experimental data, allowing to derive an average waving angle of about 37° around the MWCNT axes, and explaining the apparent discrepancy of previous experiments reported in the literature. Furthermore, we can distinguish two components in the Raman G band, associated to the longitudinal and transversal modes. Their intensity dependence as a function of polarization clearly suggests the metallic nature of these MWCNTs, experimentally verified by the valence band photoemission analysis. The present study provides a simple effective spectroscopic method to determine physico-chemical and specific morphological characteristic of carbon nanotubes.

Introduction

Since their discovery, carbon nanotubes (CNTs) have attracted huge interest in a large and varied scientific community due to their unique electronical, optical, and mechanical properties. These indeed enable a number of applications ranging from electron field emitters to batteries and quantum resistors, transistors, atomic force microscopes, mechanical memory elements, solar cells[1-15].

Single-wall carbon nanotubes (SWCNTs) have been intensively theoretically and experimentally investigated[16-24]. Their intrinsic structural anisotropy, due to the high aspect ratio,

strongly influences electrical, optical and magnetic properties, and it has been the subject of several polarization dependent Raman studies[20, 25-30]. Results show that the Raman signal intensity exhibits a maximum when the incident light is polarized along the tube axis, while it is strongly suppressed when the light is polarized perpendicular to the axis. These observations are fully explained and described by theoretical calculations on isolated SWCNTs[21, 31, 32].

Multi-wall CNTs (MWCNTs) consist of two or more SWCNTs coaxially arranged and held together by weak van der Waals interactions. A much less extent of experimental as well as theoretical efforts have been devoted to the study of these much complex systems. In particular, a strong depolarization effect has been reported in a few papers focused on polarized Raman scattering of MWCNTs[33-35]. This effect has been also observed from a rope of aligned double-wall CNTs (DWCNTs), which are special MWCNTs with only two shells[36]. Similarly to SWCNTs, the intensity of the Raman signal is indeed strongly dependent on the orientation of the polarization vector with respect to the MWCNT axes, but remarkably different angular dependences of the peak intensity have been observed[33-35]. However a specific theoretical approach is, at present, lacking. In SWCNTs, main peaks of the Raman spectrum are[37]: the G-band at ~ 1600 cm^{-1} due to vibration along the tube surface, common to graphite and graphene-like systems, the defect-induced D-band at ~ 1300-1400 cm^{-1} and their second-order modes, named G'- or 2D-band at ~ 2650 cm^{-1}, and D' band at ~ 1620 cm^{-1}. The G-band can be deconvolved into two main components, denoted G^- and G^+ (at lower and higher frequency) whose frequency separation, specific shapes, and relative intensities depend on the semiconducting/metallic character of the nanotubes[21]. The experimental observation of a multicomponent spectral feature at ~1600 cm^{-1} has been only seldom obtained in MWCNTs[38-40], and an unambiguous G^- - G^+ spectral deconvolution

is actually missing[39]. In any case, their assignment remains an open problem also because of the absence of well-developed theoretical models for multi-wall systems.

Here we report a detailed polarized Raman study on bundles of vertically aligned metallic MWCNTs grown on a silicon substrate. The high quality of the MWCNT forest, monitored by a combined microscopic and spectroscopic study, allowed us to obtain high quality Raman spectra, which only present spectral bands associated to CNT vibrations. Although nanotubes are on average highly aligned along the vertical direction at the micrometric scale, they show a non-negligible buckling at the nanometric scale. By explicitly considering the role played by this local disorder, we proposed a novel analysis of the Raman spectra, which provided an optimal agreement with present data and allowed us to solve an apparent disagreement among the previous results reported in the literature. Moreover, the detailed lineshape analysis of the spectral feature at around 1600 cm^{-1} allowed us to disentangle the D'-peak contribution at ~ 1620 cm^{-1} and, for the first time in MWCNTs, to discriminate the G^- and G^+ polarization angle dependence. These peaks have been ascribed to longitudinal optical (LO) and transversal optical (TO) modes, and the observed behaviour confirms the one theoretically predicted for metallic SWCNTs[21].

Experimental section

Conventional thermal catalytic chemical vapor technique (CCVD) was used to synthesize the vertically aligned MWCNTs[41]. Si wafers (2.0 x 2.0 cm^2) are used as substrate. First the Si substrate is covered by an Al_2O_3 layer (30 nm thickness) followed by the deposition of a thin (6 nm) Fe layer; metal sputtering deposition was used to deposited both layers. After the Fe deposition, the substrate is heated to 750 °C under hydrogen and argon flow (120 SCCM) for few minutes, the

heating causes the mobile Fe atoms to form nanoparticles that will act as catalysts for the CNT synthesis. The Ar is replaced by ethylene. The synthesis was performed using an ethylene/hydrogen mixture (50 SSCM/50 SSCM). MWCNTs of 200 μm long were obtained after ~ 20 minutes of synthesis.

SEM measurements have been carried out at the CNIS laboratory (Sapienza University), using a field-emission Zeiss Auriga 405 instrument, with a nominal resolution of 1 nm at maximum magnification, at a beam energy of 10 keV, and at a working distance of about 3.5 mm.

The XPS experiments were carried out at the LoTUS surface physics laboratory (Sapienza University) in ultra-high vacuum chambers, with base pressures in the low 10^{-10} mbar range. The photon sources for the XPS measurements were a double-anode X-ray tube and the Al K_α photon energy ($h\nu$ = 1486.7 eV). Photoelectrons were measured with a hemispherical electron analyser (VG Microtech Clam-2), using a constant pass energy mode set at 50 eV and an overall energy resolution of 1 eV. Valence band measurements were performed at the BadElph beamline of the Elettra synchrotron (Trieste, Italy) with a photon energy of 31 eV, further details in Ref.[42].

Raman measurements were carried out at the HPS laboratory (Sapienza University) using a Horiba HR-Evolution micro-spectrometer in backscattering geometry, equipped with a He-Ne laser, λ = 632.8 nm and 30 mW output power (≈15 mW at the sample surface). To avoid laser heating and sample degradation, the power on the sample was kept below 1 mW using proper optical filters. The elastically scattered light was removed by a state-of-the-art optical filtering device based on three BragGrate notch filters[43], which also allows to collect Raman spectra at very low frequencies (down to 10 cm^{-1} from the laser line). Polarization dependent Raman measurements were performed in backscattering configuration, $Y(\varepsilon_i\varepsilon_s)\overline{Y}$, using Porto notation[44]. In particular, we

exploited the so-called Vertical-Vertical (**VV**) configuration, where the polarization vectors of the incident and scattered radiation $\varepsilon_i = \varepsilon_s = \varepsilon$ were kept parallel (i.e. $Y(\boldsymbol{\varepsilon\varepsilon})\overline{Y}$). These polarization vectors were rotated by varying the angle θ between the polarization vector and the sample vertical direction, thanks to a $\lambda/2$ wave-plate placed along the laser optical path. An analyser was placed before the grating so to select the vertical component of the scattered light. The detector was a Peltier-cooled charge-coupled device (CCD) and the resolution was better than 1 cm^{-1} thanks to a 1800 grooves/mm grating with 800 mm focal length. The spectrometer was coupled with a confocal microscope supplied with a set of interchangeable objectives with long working distances and different magnifications (100X - 0.80 NA was used for the present experiment). The sample can be moved with a software-controlled mapping stage with a sub-micrometric precision for collecting automatized spectroscopic mapping. Further details on the experimental setup in Ref.[45].

Results and Discussion

MWCNTs appear highly aligned along the vertical direction with an average height of 180 μm and an average diameter of about 20 nm, as shown in the SEM image reported in Figure 1a. A single MWCNT is constituted by about 25 graphenic concentric cylinders, assuming the minimum diameter of about 2 nm for the smallest cylinder[46] and an inter-wall distance of 0.35 nm[47]. The morphology of the nanotube packing can be observed in the enlarged SEM image, shown in the inset of Figure 1a, where MWCNTs appear wavy and a zig-zag deviation from the vertical direction can be clearly observed.

Angle integrated photoemission spectra from the valence band and from the C 1s core level can identify the metallic/semiconducting state and the hybridization of the C atoms bonded in the

honeycomb lattice in the concentric cylinders of the MWCNTs. The C 1s core level spectrum (Figure 1c) shows a dominant, slightly asymmetric peak at 284.4 eV, associated to the C sp^2 hybridised bonds, with a tail towards high binding energy (BE) and a broader peak at higher BE, the latter ascribed to π-plasmon and π-π* excitation, in agreement with previous reports on MWCNTs and on graphene[48-50]. The asymmetric lineshape of the C 1s peak, apart from the expected intrinsic asymmetry due to final state effects, can also be associated to the coexistence of many components, among which the one related to the slight distortion of the sp^2 hybridization towards a sp^3-like configuration[48-50]. This is intrinsically associated to the extent of the tube curvature: the smaller is the radius, the higher is the bond distortion. We remark the absence of features at the low BE side of the C 1s core level spectra, ruling out the presence of dangling or C-H bonds[51, 52], suggesting the absence of atomic vacancies and unsaturated bonds in the MWCNT lattice.

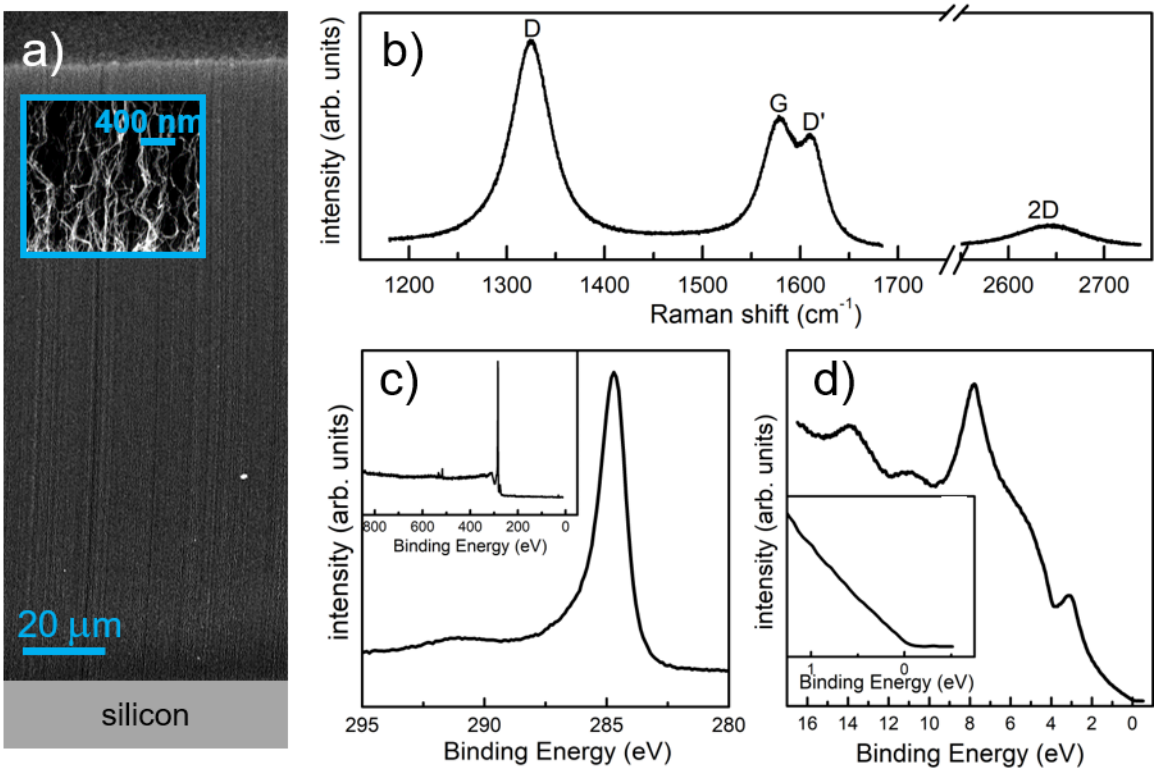

Figure 1. a) SEM image (E = 10 keV) of vertical aligned MWCNTs grown on a Si substrate, in the inset a zoomed region of the MWCNT forest; b) Raman spectrum collected at θ = 0°, i.e. with the electric field vector parallel to the CNT axis (see text); principal peak assignments are indicated by capital letters; c) XPS spectrum of the C 1s core level, with a wide binding energy range survey spectrum in the inset; d) valence band of the MWCNT sample, in the inset a zoomed energy region close to the Fermi level.

A very small C-O component, due to residual oxygen contamination of graphitic carbon is limited to about 2% [48, 53, 54], as determined by the O 1s core level observed in the general survey XPS spectrum, reported in the inset of Figure 1c.

The angle-integrated valence band spectrum of the MWCNTs allows the identification of the σ-band, at about 5.5 and 8.0 eV BE, and the π-band centred at about 3.0 eV BE. The linear dependence of the spectral density of states towards the Fermi level (inset of Figure 1d) reflects the lineshape expected on semi-metallic graphene[42, 49, 50], indicating a metallic character of these MWCNTs. It is worth noting that the surface sensitivity of the photoemitted electrons samples the outermost cylinders of the MWCNTs with a probing depth of few nanometers.

A typical Raman spectrum of the MWCNTs is shown in Figure 1b. All the expected spectral features[37, 55] can be identified, namely the D, G, D' and 2D bands, and Raman spectra collected in different position spaced by ~ 10 μm along the vertical direction are indeed actually almost identical (the spatial homogeneity of the sample on the micrometric scale is reported in Figure S2, Supporting Information). A standard fitting procedure has been applied to obtain the values for the central frequencies ν and widths W: the G-band, ν_G = 1580 cm^{-1}, W = 43 cm^{-1}, single band fitting

(sp^2 C–C stretching mode), 2D-band, ν_{2D} = 2650 cm^{-1}, W = 85 cm^{-1} (second-order mode, in-plane breathing of the hexagonal ring), the D-band, ν_D = 1325 cm^{-1}, W = 47 cm^{-1} (lattice defects), and D' band, $\nu_{D'}$ = 1614 cm^{-1}, W = 30 cm^{-1}. The 2D' peak is also measured, even if its intensity is low (see Figure S1, Supporting Information), at $\nu_{2D'}$ = 2650 cm^{-1} and W = 90 cm^{-1}. In CNTs, the D' and 2D' peaks, ascribed to lattice disorder in graphene, can be rather related to induced bond distortion, associated to the nanotube intrinsic curvature. Peak widths, as well as I_D/I_G = 2.5 and I_{2D}/I_G = 0.8 integrated intensity ratios obtained for our samples, denote high quality MWCNTs, in agreement with previous observations[37, 56]. The high-quality of the Raman spectra herewith presented allowed us to deconvolve the G-band into the G^- and G^+ spectral contributions.

A preliminary polarization analysis of the Raman spectra has been carried out, and series of Raman spectra collected from either the top (spaghetti-like nanotube arrangements[48]) or the side (vertically aligned nanotubes) of the sample at different polarization angles have been obtained and compared. No angle dependence is found for the top configuration (see Figure S3, Supporting Information), whereas a clear depolarization effect is observed for the lateral side, thus confirming a high level of nanotube alignment along the vertical direction. Based on these preliminary measurements, we focus on the study of the polarization dependent Raman spectra collected from the lateral side of the MWCNT brush, by varying the incident light polarization vector from parallel to perpendicular to the vertical direction of the CNT axes. The scattering geometry and the polarization angle θ are shown in the schematic at the bottom of Figure 2b. Spectra collected at different polarization angles ($0° < \theta < 90°$) are shown in Figure 2a over the 1225-1675 cm^{-1}

spectral range. A clear angle dependence of the spectral intensity is observed, going from a maximum of intensity at θ = 0° to a minimum at θ = 90°.

In order to quantitatively analyse the angle dependence, we defined the depolarization ratio, ρ(θ) = I(θ)/I(θ = 0°), where I(θ) is the intensity (integrated area) measured at angle θ and I(θ = 0°) is the intensity measured at θ = 0°, according to the literature[28, 33]. Using a single peak fitting for the G peak, the depolarization ratio $\rho_G(\theta)$ is calculated and shown in Figure 2b as a function of θ. A minimum value $\rho_G \approx 0.4$ is obtained for θ = 90°.

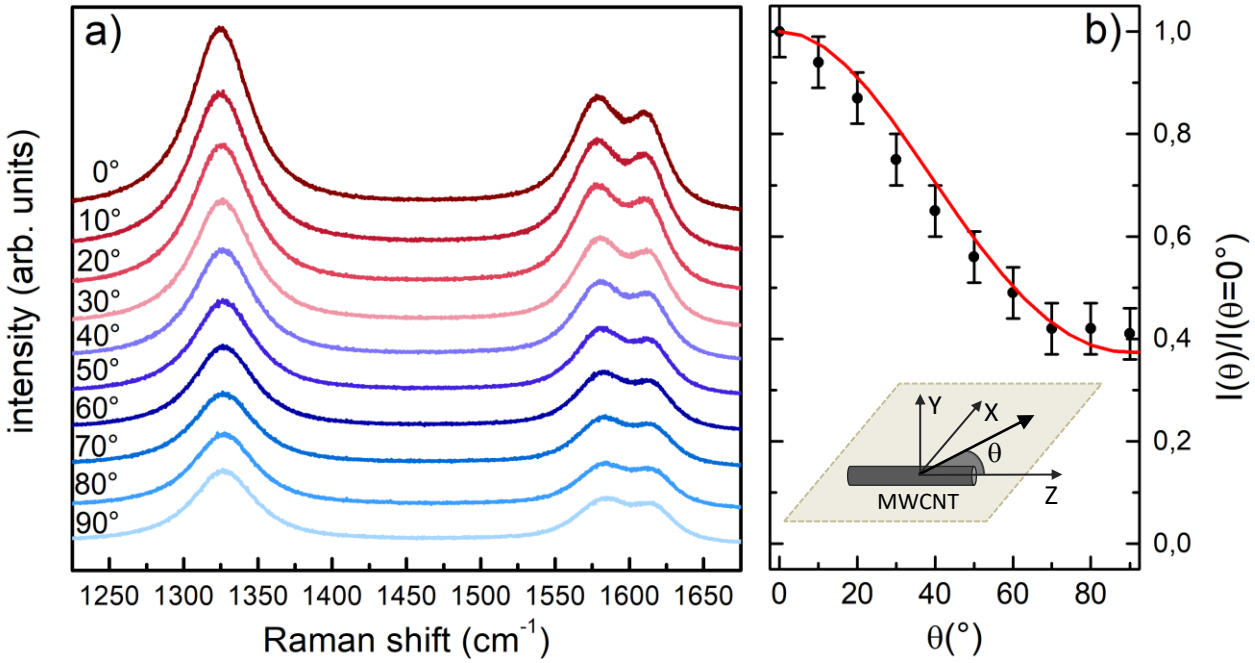

Figure 2. a) Polarization dependent Raman spectra as a function of the polarization angle θ; spectra are vertically spaced for clarity; b) spectral intensity, normalized to the θ = 0°, as a function of polarization (dots); the red curve represents the fitting function $I_M(\theta)$ (see text for details). A

schematic of the scattering geometry for a single straight MWCNT is shown at the bottom of panel b).

A theoretical angle dependence of the Raman intensity can be found using the following equation:

$$I_G \propto |\boldsymbol{\varepsilon_i} \cdot R_G \cdot \boldsymbol{\varepsilon_s}|^2 \quad (1)$$

where R_G is the Raman tensor for the G-mode[31, 33] (nanotube axis is along z direction):

$$R_G = \begin{pmatrix} -\frac{1}{2} & 0 & 0 \\ 0 & -\frac{1}{2} & 0 \\ 0 & 0 & 1 \end{pmatrix} \quad (2)$$

and ε_i and ε_s are the polarization vectors of the incident and the scattered light respectively. In **VV** configuration, i.e. $Y(\boldsymbol{\varepsilon\varepsilon})\overline{Y}$ using the Porto notation, we have:

$$\boldsymbol{\varepsilon_i} = \boldsymbol{\varepsilon_s} = \boldsymbol{\varepsilon} = \begin{pmatrix} \sin\theta \\ 0 \\ cos\theta \end{pmatrix} \quad (3)$$

From equations (1) and (2), the angular dependence of the Raman intensity and the depolarization ratio can be obtained[31]:

$$\rho_G(\theta) = \frac{I_G(\theta)}{I_G(\theta=0°)} = (cos^2\theta - \frac{1}{2}\, sin^2\theta)^2 = \frac{1}{4}\,(3\, cos^2\theta - 1)^2 \quad (4)$$

This equation provides a minimum value:

$$\rho_G(\theta_{min}) = 0 \quad (5a)$$

for:

$$\theta_{min} = arccos\left(\frac{1}{\sqrt{3}}\right) \cong 57° \quad (5b)$$

This approach does not reproduce the present results since data show a clear minimum different from zero at $\theta_{min} = 90°$. This difference can arise from the intrinsic morphology of the MWCNT samples analysed. In the present case, indeed, the sample consists of vertical bundles of wavy nanotubes. Therefore, the angle between the nanotube axes and the polarization vector of the incident radiation cannot be strictly defined on a small spatial scale. Taking into account the local deviation of the nanotube axes from the vertical direction, a weighted average of polarization angles should be considered rather than a single value.

Drawing on the strategy previously proposed for SWCNTs in composites[57], we introduce a Gaussian distribution $g(\theta)$ for the polarization angles and calculate the convolution integral to estimate the angle dependence of the Raman intensity I_M, as follows:

$$I_M(\theta) = \int_{-\infty}^{+\infty} \rho(\theta')g(\theta - \theta')d\theta' \quad (6)$$

where

$$g(\theta - \theta') = \frac{1}{\sqrt{2\pi}\,\sigma}\, e^{-\frac{(\theta-\theta')^2}{2\sigma^2}} \quad (7)$$

In this convolution integral, σ results to be the only parameter, representing an estimate of the nanotube axis angular deviation from the vertical direction. The σ value giving the best agreement with the experimental angular dependence results to be $\theta = 37° \pm 4°$, where the error value is an

empirical estimate obtained as the maximum variation of the parameter providing a theoretical curve still fitting within the experimental error bars. As reported in Figure 2b, the comparison between the calculated curve and the experimental data is very good.

In the literature, contrasting results about the angle dependence of the depolarization ratio have been obtained, though. In particular, a minimum value, $\rho_{min} \sim 0$, has been found at $\theta_{min} \sim 57°$ in Ref.[33], whereas more or less pronounced minima, $\rho_{min} \sim 0$ for Ref.[34] and $\rho_{min} \sim 0.25$ for Ref.[35], are reached at $\theta_{min} \sim 90°$. The absence of a theoretical approach specifically developed for MWCNTs makes the realization of a coherent framework even more complex. The experimental data shown in Ref.[33] have been modelled exploiting the theory for SWCNTs of Ref.[31], which predicted $\rho_{min} = 0$ at $\theta_{min} = 57°$, despite the not optimal experimental/theoretical agreement (see Figure S7, Supporting Information). In Ref.[34] the same theory has been slightly modified introducing an empirical attenuation parameter for light polarized perpendicular to the nanotube axis, which accounts for both $\rho_{min} \sim 0$ and $\theta_{min} \sim 90°$ [58]. In Ref.[35], the same explanation has been provided even if a ρ_{min} value significantly deviates from the predicted zero value.

It is worth to underline that the different morphology of the measured samples, namely an isolated CNT[34] and a bundle of aligned MWCNTs[33, 35], could definitely affect the polarization response. We thus attempted to extend our approach also in the case of literature data, and, by fitting the experimental data reported in Ref.[33], we obtain a good agreement (see Figure S7, Supporting Information) and a value $\sigma = 42° \pm 4°$, comparable with the present results. Good results have been obtained for experimental data from Ref.[35], with $\sigma = 45°$ (see Figure S7, Supporting Information). A comparison of our results with those obtained from a DWCNT sample[36] is also reported in Figure S8 (Supporting Information), where an almost perfect agreement is observed. It

is clear, on the other hand, that the present procedure cannot be applied to the data of Ref.[34] since in that case the polarization angle is well defined. Apart from correctly reproducing all the experimental data, the present approach allows us to determine the σ parameter, which can be considered as an estimation of the misalignment factor. The wide range of comparison we show in the Supporting Information makes us confident about the large validity of our approach.

A close inspection of the angle dependence of the central frequency of the G-band allows to highlight a progressive, small but significant, frequency shift. Going from θ = 0° to θ = 90°, the frequency shifts from 1577 cm^{-1} to 1583 cm^{-1}, well beyond the experimental uncertainty (see Figure S4, Supporting Information). This behaviour cannot be explained considering a single component for the G-band; however, if we consider the G-band as composed of the two longitudinal and transverse G^- and G^+ components[21, 37, 39], the observed data can be explained. Taking this in consideration, we fitted the spectra over the 1450-1680 cm^{-1} spectral region using three Voigt contributions ascribed to the G^-, G^+ and D' vibrational modes, respectively. The very good agreement between the best-fit curve and the experimental data is shown in Figure 3 for θ = 0° and θ = 90°. It is worth to notice that in the single-peak fit procedure the G-band is well described by an almost full Gaussian curve, whereas in the case of two contributions, G^- and G^+, it presents an almost full natural Lorentzian profile. This can be considered a further evidence of the G^- - G^+ presence, previously brought to light for SWCNTs[21, 37], also in MWCNTs. In order to reduce the number of the fitting parameters, the third contribution ascribed to the D' peak was kept fixed, both in frequency and in width.

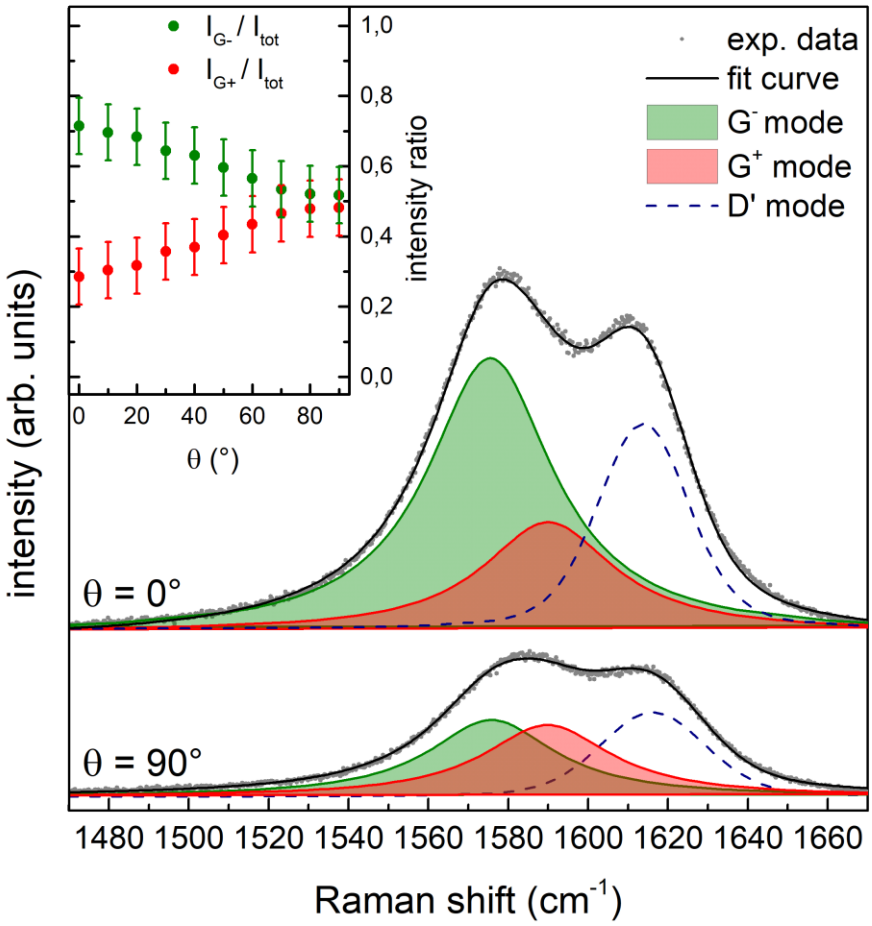

Figure 3. Raman spectra of MWCNT over the 1480-1680 cm^{-1} spectral range (gray dots) at $\theta = 0°$ and $\theta = 90°$, along with the best fit curves: the green peak is associated to the G^- mode, the red one is associated to G^+, and the yellow one represents the D' mode. In the inset, the intensity ratios for G^- and G^+ are reported as a function of θ.

In the fitting procedure, the difference of frequency between G^- and G^+ was also kept fixed, so that the spectral weights of G^- and G^+ components are the only parameters that can change. Very similar results were obtained even keeping the frequency difference of G^- and G^+ free in the fitting analysis.

The intensity ratio for G^- and G^+ is defined as follows:

$$\frac{I_{G^-/G^+}(\theta)}{I_{tot}\,(\theta)}$$

where $I_{G-/G+}(\theta)$ is the integrated area of the G^-/G^+ peak and I_{tot} is the sum of the integrated area of the three peaks used in the fitting analysis. Note that their intensity ratios are complementary: at $\theta = 0°$, when the polarization of the incident radiation is parallel to the tube axes, G^- reaches the maximum intensity while G^+ the minimum; at $\theta = 90°$, when the polarization of the incident radiation is perpendicular to the tube axes, they tend to the same value.

As already mentioned in the introduction, the origin of the G^-/G^+ splitting of the G peak in SWCNTs can be traced back to the combined effects of dynamic, curvature and confinement[21]. For both metallic and semiconducting SWCNTs, the position of the G^- peak depends on the tube diameter, having lower frequency for smaller diameters, while the position of the G^+ peak is substantially diameter independent[21]. A direct effect of the metallic nature of the nanotubes can be instead found in the G^-/G^+ peak assignment. DFT calculations within the approximation of Electron Zone Folding, which accounts for the electron-phonon coupling, have shown that $\nu_{LO} > \nu_{TO}$ for semiconducting SWCNTs, while $\nu_{LO} < \nu_{TO}$ for metallic ones, where ν_{LO} (ν_{TO}) is the frequency associated to the longitudinal (transversal) optical mode[21]. Bearing in mind that conventionally the G^+ peak has a central frequency higher than that of the G^-, DFT results thus provide an assignment of G peaks in metallic tubes opposite to that in semiconducting ones. This has been demonstrated for SWCNTs by reporting the G^-/G^+ experimental and theoretical frequencies as a function of the tube diameter for metallic and semiconducting tubes[21].

Our results (1576 cm^{-1} for G^- and 1589 cm^{-1} for G^+), although obtained from MWCNTs, well compare with those reported for metallic SWCNTs at the highest diameters (i.e. around 2 nm,

which is the estimated internal tube diameter of present MWCNTs). Moreover, the Raman analysis reported in the inset of Figure 3 shows that the intensity of the G^- peak is much higher than that of the G^+ peak when the incident polarization vector is parallel to the tube axis ($\theta = 0°$). This is in a straightforward agreement with the assignment for metallic SWCNTs that is the LO mode for G^- and TO mode for G^+. Apart from the specific findings, all the present experimental results thus coherently support the idea that the theory developed for single-wall nanotubes can be safely extended to the multi-wall systems.

Conclusions

A detailed polarization dependent Raman analysis has been carried out on bundles of vertically aligned metallic MWCNTs grown on a silicon substrate. The combined use of microscopic and spectroscopic techniques showed that MWCNTs are on the average highly aligned along the vertical direction at the micrometric scale. However, on a smaller spatial scale, they result to be significantly misaligned with respect to the average tube axis direction. In order to account for this effect, we introduced a misalignment parameter σ, which allowed us to calculate the expected values of the G-peak intensity for a bundle of slightly buckled tubes, resulting in an average waving angle of 37° across the vertical direction. The calculated curve results to be in a very good agreement with the measured intensity as a function of θ. It is worth to notice that the same approach allowed us to solve apparently conflicting experimental results reported in the literature for the angular behaviour of the G-peak intensity (see and compare present results and Refs.[33-35]). Moreover, the identification of a quantitative parameter, related to the misalignment on the local scale, could play an important role in the characterization of MWCNT bundles, in particular when they are used as part of a highly directional detector (e.g. for dark matter[48]).

The polarization analysis of the Raman signal also allowed the identification of the metallic nature of our MWCNTs. Indeed, the G^- and G^+ components of peak G are associated to the longitudinal and transversal optical modes and their assignment is strictly related to the metallic/semiconducting nature of the system. The present results showed that the G^- peak (longitudinal mode) is more intense when the incident polarization vector is parallel to the tube axis, whereas the G^+ peak (transversal mode) reaches its maximum when the incident polarization vector is perpendicular to the tube axis.

These results demonstrate a new important diagnostic capability of the Raman spectroscopy for this kind of systems and, as a whole, they are in very good agreement with the theoretical predictions reported for SWCNTs. This good agreement suggests a crucial role of the inner tube in determining the properties of the whole MWCNT brush and asks for a specific theoretical investigation focused to multi-wall systems.

Supporting Information

Sample characterization, polarization analysis of the Raman spectra, and comparison with literature.

Acknowledgements

We acknowledge the Physics Department of Sapienza University for funding and providing access to the CNIS Center for Nanotechnology and Innovation. CB is Research Associate at the FRS-FNRS (Belgium). We thank Simone Di Cataldo for useful discussion and Francesco Mura for his technical support with SEM measurements.

References

(1) Saito, R.; R. Saito, Dresselhaus, G.; Dresselhaus, M.S. Physical properties of carbon nanotubes. *Imperial College Press: London,* **1998**.

(2) Saito, Y.; Hamaguchi, K.; Uemura S.; Uchida, K.; Tasaka, Y.; Ikazaki, F.; Yumura, M.; Kasuya, A.; Nishina, Y. Field emission from multi-walled carbon nanotubes and its application to electron tubes. *Appl. Phys. A: Mater. Sci. Process.* **1998**, *67*, 95-100.

(3) Baughman, R.H.; Zakhidov, A.A.; De Heer, W.A. Carbon nanotubes-the route toward applications. *Science* **2002**, *297*, 787-792.

(4) Jorio, A.; Dresselhaus, G.; Dresselhaus, M.S. Carbon nanotubes: advanced topics in the synthesis, structure, properties and applications. *Springer Science & Business Media: New York,* **2007**.

(5) Kempa, K.; Rybczynski, J.; Huang, Z.; Gregorczyk, K.; Vidan, A.; Kimball, B.; Carlson, J.; Benham, G.; Wang, Y.; Herczynski, et al. Carbon nanotubes as optical antennae. *Adv. Mater.* **2007**, *19*, 421−426.

(6) Avouris, P.; Freitag, M.; Perebeinos, V. Carbon-nanotube photonics and optoelectronics. *Nat. Photonics* **2008**, *2*, 341-350.

(7) Wang, F.; Rozhin, A. G.; Scardaci, V.; Sun, Z.; Hennrich, F.; White, I.H.; Milne, W.I. Ferrari, A.C. Wideband-Tuneable, Nanotube Mode-Locked, Fibre Laser. *Nat. Nanotechnol.* **2008**, *3*, 738−742.

(8) Song, Y.W.; Yamashita, S.; Maruyama, S. Single-walled carbon nanotubes for high-energy optical pulse formation. *Appl. Phys. Lett.* **2008**, 92, 021115.

(9) De Volder, M.F.L.; Tawfick, S.H.; Baughman, R.H.; Hart, A.J. Carbon nanotubes: present and future commercial applications. *Science* **2013**, *339*, 535-539.

(10) Ulisse, G.; Brunetti, F.; Tamburri, E.; Orlanducci, S.; Cirillo, M.; Terranova, M.L.; Di Carlo, A. Carbon nanotube cathodes for electron gun. *IEEE Electron Device Lett.* **2013**, *34*, 698-700.

(11) Capparelli, L.M.; Cavoto, G.; Mazzilli, D.; Polosa, A.D. Directional dark matter searches with carbon nanotubes. *Phys. Dark Universe* **2015**, *9-10*, 24-30.

(12) Zhu, Z. An overview of carbon nanotubes and graphene for biosensing applications. *Nano-micro Lett.* **2017**, *9*, 25.

(13) Jeon, I.; Seo, S.; Sato, Y.; Delacou, C.; Anisimov, A.; Suenaga, K.; Kauppinen, E.I.; Maruyama, S.; Matsuo, Y. Perovskite solar cells using carbon nanotubes both as cathode and as anode. *J. Phys. Chem. C* **2017**, 121, 25743-25749

(14) Jeon, I.; Xiang, R.; Shawky, A.; Matsuo, Y.; Maruyama S. Single-walled carbon nanotubes in emerging solar cells: synthesis and electrode applications. *Adv. Energy Mater.* **2018**, 1801312

(15) Cavoto, G.; Luchetta, F.; Polosa, A.D. Sub-GeV dark matter detection with electron recoils in carbon nanotubes. *Phys. Lett. B* **2018**, 776, 338-344.

(16) McEuen, P.L. Single-wall carbon nanotubes. *Phys. World* **2000**, *13*, 31-35.

(17) Zhou, C.; Kong, J.; Daiet, H. Electrical measurements of individual semiconducting single-walled carbon nanotubes of various diameters. *Appl. Phys. Lett.* **2000**, *76*, 1597-1599.

(18) Jorio, A.; Saito, R.; Hafner, J.H.; Lieber, C.M.; Hunter, M.; McClure, T.; Dresselhaus, G.; Dresselhaus, M.S. Structural (n, m) determination of isolated single-wall carbon nanotubes by resonant Raman scattering. *Phys. Rev. Lett.* **2001**, *86*, 1118-1121.

(19) Bachilo, S.M.; Strano, M.S.; Kittrell, C.; Hauge, R.H.; Smalley, R.E.; Weisman, R.B. Structure-assigned optical spectra of single-walled carbon nanotubes. *Science* **2002**, 298, 2361-2366.

(20) Jorio, A.; Souza Filho, A.G.; Brar, V.W.; Swan, A.K.; Ünlü, M.S.; Goldberg, B.B.; Righi, A.; Hafner, J.H.; Lieber, C.M.; Saito, R. et al. Polarized resonant Raman study of isolated single-wall carbon nanotubes: Symmetry selection rules, dipolar and multipolar antenna effects. *Phys. Rev. B* **2002**, *65*, 121402.

(21) Piscanec, S.; Lazzeri, M.; Robertson, J.; Ferrari, A.C.; Mauri, F. Optical phonons in carbon nanotubes: Kohn anomalies, Peierls distortions, and dynamic effects. *Phys. Rev. B* **2007**, *75*, 035427.

(22) Murakami, Y.; Maruyama, S. Effect of dielectric environment on the ultraviolet optical absorption of single-walled carbon nanotubes. *Phys. Rev. B* **2009**, 79, 155445.

(23) Anoshkin, I.V.; Nefedova, I.I.; Lioubtchenko, D.V.; Nefedov, I.S.; Räisänen, A.V. Single walled carbon nanotube quantification method employing the Raman signal intensity. *Carbon* **2017**, *116*, 547-552.

(24) Dixit, S.; Shukla, A.K. Raman studies of single-walled carbon nanotubes synthesized by pulsed laser ablation at room temperature. *Appl. Phys. A* **2018**, *124*, 400.

(25) Hwang, J.; Gommans, H.; Ugawa, A.; Tashiro, H.; Haggenmueller, R.; Winey, K.I.; Fischer, J.E.; Tanner, D.B.; Rinzler, A.G. Polarized spectroscopy of aligned single-wall carbon nanotubes. *Phys. Rev. B* **2000**, 62, 13310-13313.

(26) Duesberg, G.S.; Loa, I.; Burghard, M.; Syassen, K.; Rothet, S. Polarized Raman spectroscopy on isolated single-wall carbon nanotubes. *Phys. Rev. Lett*. **2000**, *85*, 5436-5439.

(27) Jorio, A.; Dresselhaus, G.; Dresselhaus, M.S.; Souza, M.; Dantas, M.S.S.; Pimenta, M.A.; Rao, A.M.; Saito, R.; Liu, C.; Chenget, H.M. Polarized Raman study of single-wall semiconducting carbon nanotubes. *Phys. Rev. Lett.* **2000**, *85*, 2617-2620.

(28) Gommans, H.H.; Alldredge, J.W.; Tashiro, H.; Park, J.; Magnuson, J.; Rinzler, A.G.; Fibers of aligned single-walled carbon nanotubes: Polarized Raman spectroscopy. *J. Appl. Phys.* **2000**, 88, 2509-2514.

(29) Zhang, Z.; Einarsson, E.; Miyauchi, Y.; Maruyama, S. Polarization dependence of radial breathing mode peaks in resonant Raman spectra of vertically aligned single-walled carbon nanotubes. *Phys. Rev. B*, **2010**, 81, 165442.

(30) Kramberger, C.; Thurakitseree, T.; Chiashi, S.; Einarsson, E.; Maruyama, S. On the polarization-dependent Raman spectra of aligned carbon nanotubes. *Appl. Phys. A* **2012**, 109, 509–513.

(31) Saito, R.; Takeya, T.; Kimura, T.; Dresselhaus, G.; Dresselhaus, M.S. Raman intensity of single-wall carbon nanotubes. *Phys. Rev. B* **1998**, *57*, 4145-4153.

(32) Dresselhaus, M.S.; Dresselhaus, G.; Jorio, A.; Souza Filho, A.G.; Saito, R. Raman spectroscopy on isolated single wall carbon nanotubes. *Carbon* **2002**, *40*, 2043–2061.

(33) Rao, A.M.; Jorio, A.; Pimenta, M.A.; Dantas, M.S.S.; Saito, R.; Dresselhaus, G.; Dresselhaus, M.S. Polarized Raman study of aligned multiwalled carbon nanotubes. *Phys. Rev. Lett.* **2000**, *84*, 1820-1823.

(34) Zdrojek, M.; Judek, J.; Wąsiket, M. Laser Heating Control with Polarized light in isolated multiwalled carbon nanotubes. *Phys. Rev. Lett.* **2012**, *108*, 225501.

(35) Yang, X.; Yao, M.; Lu, W.; Chen, S.; Du, M.; Zhu, L.; Li, H.; Liu, R.; Cui, T.; Sundqvist, B.; et al. Polarized Raman study of aligned multiwalled carbon nanotubes arrays under high pressure. *J. Phys. Chem. C* **2015**, 119, 27759−27767.

(36) Ren, W.; Li, F.; Cheng, H.M. Polarized Raman analysis of aligned double-walled carbon nanotubes. *Phys. Rev. B* **2005**, *71*, 115428.

(37) Dresselhaus, M.S.; Dresselhaus, G.; Saito, R.; Jorio, A. Raman spectroscopy of carbon nanotubes. *Phys. Rep.* **2005**, *409*, 47–99.

(38) Chhowalla, M.; Ferrari, A.C.; Robertson, J.; Amaratunga, G.A.J. Evolution of sp^2 bonding with deposition temperature in tetrahedral amorphous carbon studied by Raman spectroscopy. *Appl. Phys. Lett.* **2000**, *76*, 1419-1421.

(39) Lehman, J.H.; Terrones, M.; Mansfield, E.; Hurst, K.E.; Meunierg, V. Evaluating the characteristics of multiwall carbon nanotubes. *Carbon* **2011**, *49*, 2581-2602.

(40) Hirschmann, T.C.; Dresselhaus, M.S.; Muramatsu, H.; Seifert, M.; Wurstbauer, U.; Parzinger, E.; Nielsch, K.; Ahm Kim, Y.; Araujo, P.T. G' band in double- and triple-walled carbon nanotubes: a Raman study. *Phys. Rev. B* **2015**, *91*, 075402.

(41) Chhowalla, M.; Ducati, C.; Rupesinghe, N.L.; Teo, K.B.K.; Amaratunga, G.A.J. Field emission from short and stubby vertically aligned carbon nanotubes. *Appl. Phys. Lett.* **2001,** *79*, 2079.

(42) Scardamaglia, M.; Struzzi, C.; Aparicio Rebollo, F.J.; De Marco, P.; Mudimela, P.R.; Colomer, J.F.; Amati, M.; Gregoratti, L.; Petaccia, L.; Snyders, R.; et al. Tuning electronic properties of carbon nanotubes by nitrogen grafting: chemistry and chemical stability, *Carbon* **2015**, *83*, 118-127.

(43) Glebov, A.L.; Mokhun, O.; Rapaport, A.; Vergnole, S.; Smirnov, V.; Glebov, L.B. Volume Bragg gratings as ultra-narrow and multiband optical filters, Proc. SPIE 8428, 84280C, Micro-Optics **2012**.

(44) Porto, S.P.S.; Giordmaine, J.A.; Damen, T.C. Depolarization of Raman scattering in calcite. *Phys. Rev.* **1966**, *147*, 608-611.

(45) Capitani, F.; Koval, S.; Fittipaldi, R.; Caramazza, S.; Paris, E.; Mohamed, W.S.; Lorenzana, J.; Nucara, A.; Rocco, L.; Vecchione, A.; et al. Raman phonon spectrum of the Dzyaloshinskii-Moriya helimagnet $Ba_2CuGe_2O_7$. *Phys. Rev. B* **2015**, *91*, 214308.

(46) Guan, L.; Suenaga, K.; Iijima. S. Smallest carbon nanotube assigned with atomic resolution accuracy. *Nano Lett.* **2008**, *8*, 459–462.

(47) Pauling, L. The Nature of the Chemical Bond. *Cornell University Press*, **1960**.

(48) D'Acunto, G. Ripanti, F.; Postorino, P.; Betti, M.G.; Scardamaglia, M.; Bittencourt, C.; Mariani, C. Channelling and induced defects at ion-bombarded aligned multiwall carbon nanotubes. *Carbon* **2018**, *139*, 768-775.

(49) Di Bernardo, I.; Avvisati, G.; Mariani, C.; Motta, N.; Chen, C.; Avila, J.; Asensio, M.C.; Lupi, S.; Ito, Y.; Chen, M.; et al. Two-dimensional hallmark of highly interconnected three-dimensional nanoporous graphene. *ACS Omega* **2017**, *2*, 3691-3697.

(50) Di Bernardo, I.; Avvisati, G.; Chen, C.; Avila, J.; Asensio, M.C.; Hu, K.; Ito, Y.; Hines, P.; Lipton-Duffin, J.; Rintoul, L.; et al. Topology and doping effects in three-dimensional nanoporous graphene. *Carbon* **2018**, *131*, 258-265.

(51) Massimi, L.; Angelucci, M.; Gargiani, P.; Betti, M.G.; Montoro, S.; Mariani, C. Metal-phthalocyanine ordered layers on Au(110): Metal-dependent adsorption energy. *J. Chem. Phys.* **2014**, *140*, 244704.

(52) Massimi, L.; Ourdjini, O.; Lafferentz, L.; Koch, M.; Grill, L.; Cavaliere, E.; Gavioli, L.; Cardoso, C.; Prezzi, D.; Molinari, E.; et al. Surface-assisted reactions toward formation of graphene nanoribbons on Au(110) surface. *J. Phys. Chem. C* **2015**, *119*, 2427-2437.

(53) Estrade-Szwarckopf, H. XPS photoemission in carbonaceous materials: a "defect" peak beside the graphitic asymmetric peak. *Carbon* **2004**, *42*, 1713-1721.

(54) Mezzi, A.; Kaciulis, S. Surface investigation of carbon films: from diamond to graphite. *Surf. Interface Anal.* **2010**, *42*, 1082-1084.

(55) Thess, A.; Lee, R.; Nikolaev, P.; Dai, H.; Petit, P.; Robert, J.; Xu, C.; Hee Lee, Y.; Gon Kim, S.; Rinzler, A.G.; et al. Crystalline ropes of metallic carbon nanotubes. *Science* **1996**, *273*, 483-487.

(56) Dresselhaus, M.S.; Jorio, A.; Hofmann, M.; Dresselhaus, G.; Saito, R. Perspectives on carbon nanotubes and graphene Raman spectroscopy. *Nano Lett.* **2010**, *10*, 751-758.

(57) Haggenmueller, R.; Gommans, H.H.; Rinzler, A.G.; Fischer, J.E.; Winey, K.I. Aligned single-wall carbon nanotubes in composites by melt processing methods. *Chem. Phys. Lett.* **2000** *330*, 219-225.

(58) Ajiki, H.; Ando, T. Aharonov-Bohm effect in carbon nanotubes. *Physica B* **1994**, *201*, 349-352.

TOC Graphic

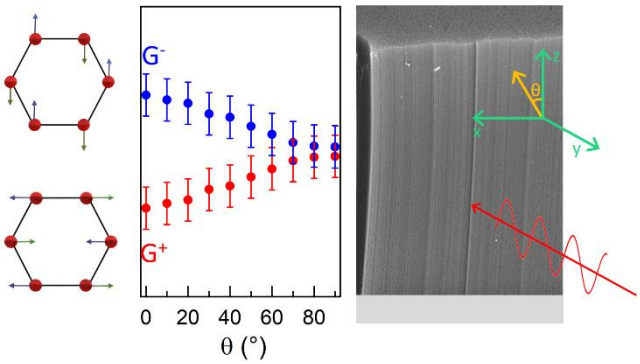

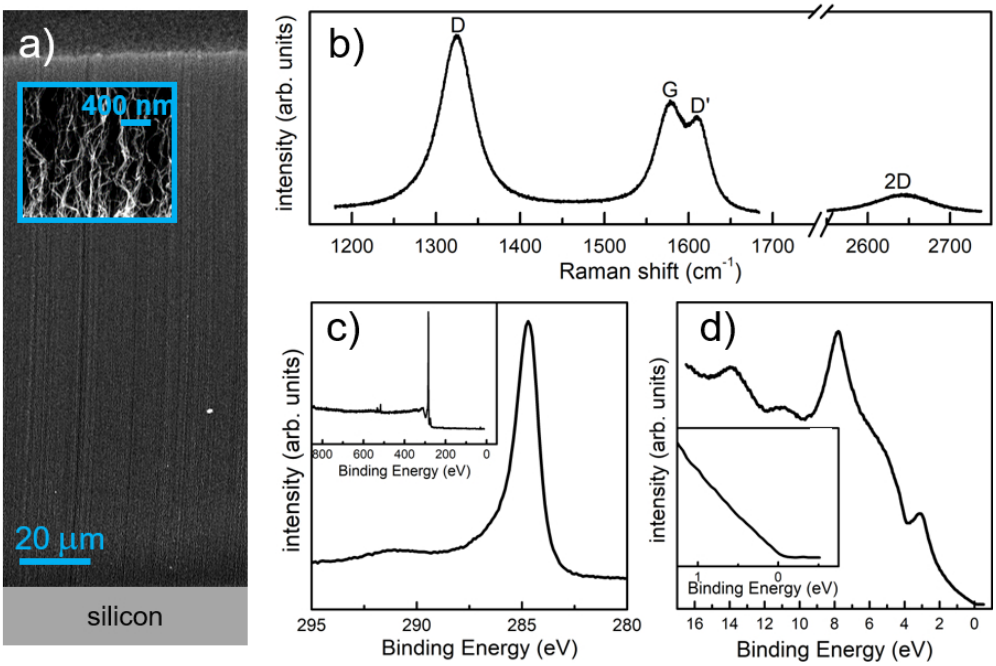

Figure 1. a) SEM image (E = 10 keV) of vertical aligned MWCNTs grown on a Si substrate, in the inset a zoomed region of the MWCNT forest; b) Raman spectrum collected at θ = 0°, i.e. with the electric field vector parallel to the CNT axis (see text); principal peak assignments are indicated by capital letters; c) XPS spectrum of the C 1s core level, with a wide binding energy range survey spectrum in the inset; d) valence band of the MWCNT sample, in the inset a zoomed energy region close to the Fermi level.

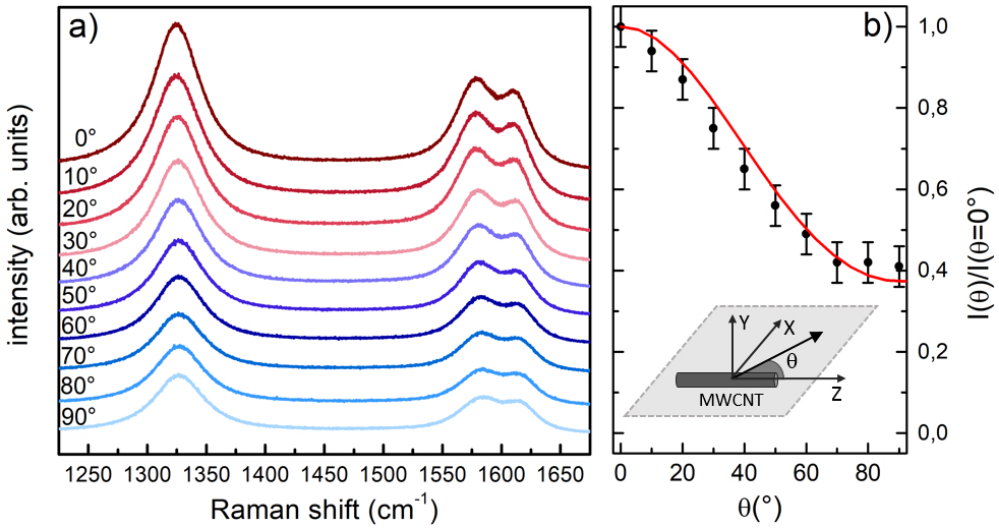

Figure 2. a) Polarization-dependent Raman spectra, as a function of the polarization angle θ; spectra are vertically spaced for clarity; b) spectral intensity, normalized to the θ = 0°, as a function of polarization (dots); the red curve represents the fitting function IM(θ) (see text for details). A schematic of the scattering geometry for a single straight MWCNT is shown at the bottom of panel b).

166x87mm (150 x 150 DPI)

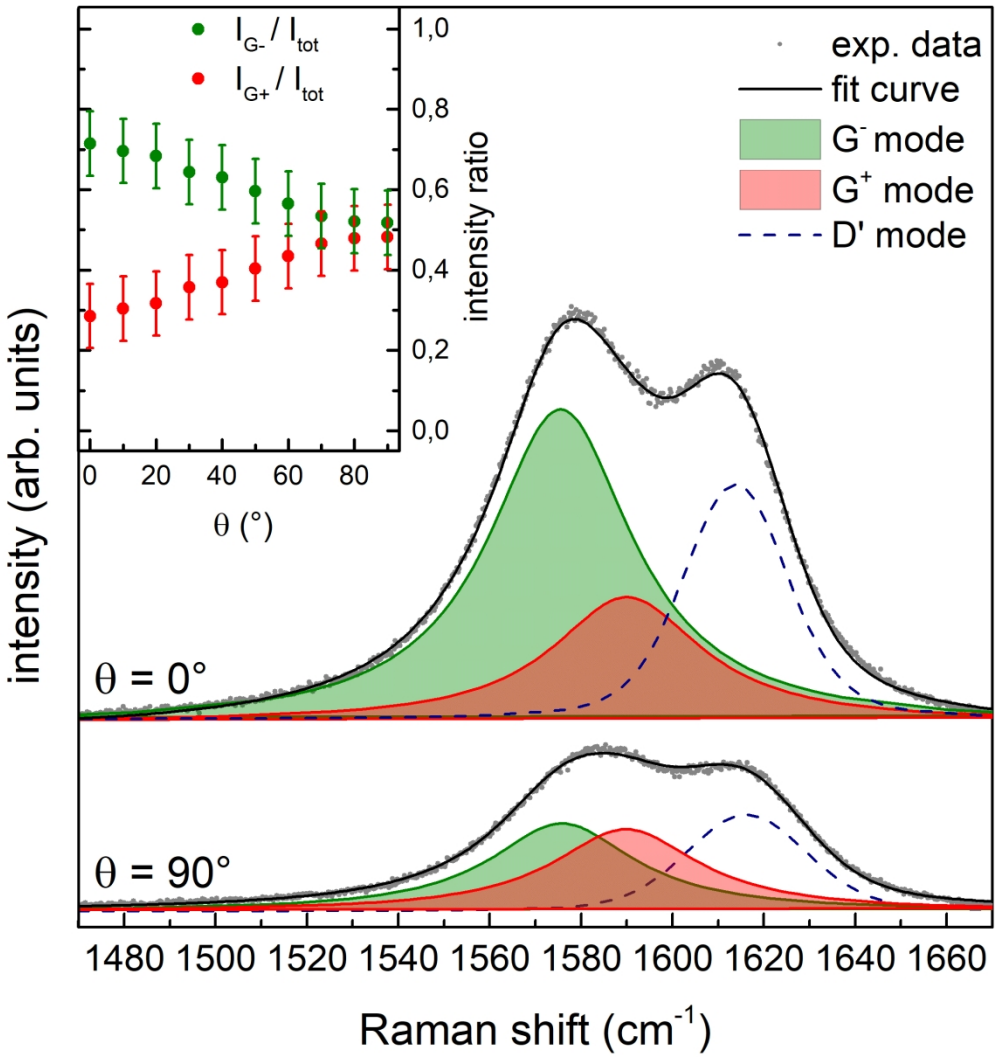

Figure 3. Raman spectra of MWCNT over the 1480-1680 cm-1 spectral range (gray dots) at θ=0° and θ=90°, along with the best fit curves: the green peak is associated to the G– mode, the red one is associated to G+, and the yellow one represents the D' mode. In the inset, the intensity ratios for G- and G+ are reported as a function of θ.

190x200mm (300 x 300 DPI)